




Article

Integrated Photogrammetric-Acoustic Technique for Qualitative Analysis of the Performance of Acoustic Screens in Sandy Soils

José M. Bravo ¹, Fernando Buchón-Moragues ^{2,*}, Javier Redondo ³, Marcelino Ferri ¹ and Juan V. Sánchez-Pérez ¹

¹ Centro de Tecnologías Físicas, Acústica, Materiales y Astrofísica, División Acústica, Universitat Politècnica de València, Camino de Vera s/n, 46022 Valencia, Spain; jobrapla@upv.es (J.M.B.); mferri@upv.es (M.F.); jusanc@fis.upv.es (J.V.S.-P.)

² Departamento de Ingeniería Cartográfica, Geodesia y Fotogrametría, Universitat Politècnica de València, Camino de Vera s/n, 46022 Valencia, Spain

³ Instituto de Investigación para la Gestión Integrada de zonas Costeras, Universitat Politècnica de València, Paraninf 1, Grao de Gandia, 46730 Valencia, Spain; fredondo@upv.es

* Correspondence: fbuchon@upv.es; Tel.: +34-660-674-946

Received: 27 September 2019; Accepted: 7 November 2019; Published: 8 November 2019



Abstract: In this work, we present an integrated photogrammetric-acoustic technique that, together with the construction of a scaled wind tunnel, allows us to experimentally analyze the permeability behavior of a new type of acoustic screen based on a material called sonic crystal. Acoustic screens are devices used to reduce noise, mostly due to communication infrastructures, in its transmission phase from the source to the receiver. The main constructive difference between these new screens and the classic ones is that the first ones are formed by arrays of acoustic scatterers while the second ones are formed by continuous walls. This implies that, due to their geometry, screens based on sonic crystals are permeable to wind and water, unlike the classic ones. This fact may allow the use of these new screens in sandy soils, where sand would pass through the screen, avoiding the formation of sand dunes that are formed in classic screens and drastically reducing their acoustic performance. In this work, the movement of the sand and the resulting acoustic attenuation in these new screens are analyzed qualitatively, comparing the results with those obtained with the classic ones, and obtaining interesting results from the acoustic point of view.

Keywords: photogrammetry; noise control; acoustic barriers; sonic crystal

1. Introduction

Noise can be defined as an unwanted or unpleasant outdoor sound generated by human activity, and is one of the main environmental problems all over the world [1]. This kind of pollution can be controlled in each of the three phases into which its propagation is divided: (i) Noise generation at the source; (ii) transmission of noise from the source to the receiver, and (iii) noise reception. The most useful solution to control noise in its phase of transmission from the source to the receiver is the use of acoustic barriers or acoustic screens (ABs). In Figure 1a, one can see an outline of the acoustic performance of these devices. Classical ABs are formed by continuous rigid material with a minimum superficial density of 20 kg/m² [2] (see an example in Figure 1b). However, these classical ABs present some drawbacks related with aesthetic and communication problems along with their limited technological performance in noise control, as they are not able to discriminate between types of sound and therefore the same AB is used to attenuate very different noises [3,4]. In order to obtain ABs with high noise control performance, new advanced materials called sonic crystals are being used,

with the ABs formed by these materials called sonic crystal acoustic screens (SCASs). Sonic crystals can be defined as a heterogeneous material consisting of periodic arrays of acoustic scatterers embedded in air [5] (see Figure 1c). A great effort has been made to analyze the physical properties of these new materials and to apply them to the field of environmental acoustics due to their excellent properties in noise control [6–8], or to analyze their behavior regarding wave propagation in viscoelastic materials instead of in air [9,10]. One of these interesting properties is their permeability to wind and water as they are discontinuous materials. This permeability can help the placement of ABs in environments that until now were forbidden, as is the case of desert areas, where there is significant transportation of sand due to the existing wind. However, this possibility requires the use of specific techniques to estimate the volume of sand displaced in the presence of SCASs with great precision.

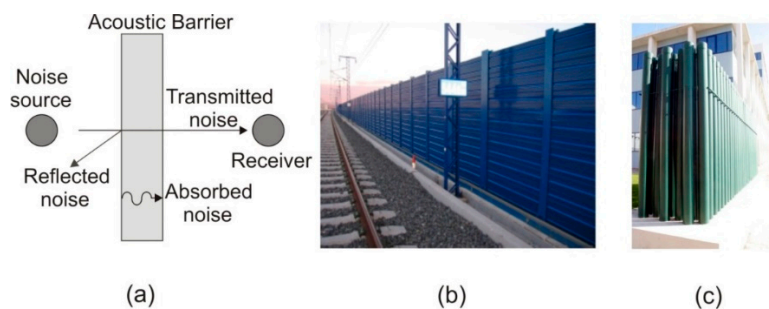


Figure 1. (a) Plan view of the acoustic performance of an Acoustic Barrier (AB); (b) Image of a classic acoustic barrier, made with a continuous surface, in the surroundings of a railway; (c) Picture of a SCAS made up with rigid cylinders as scatterers, where its transparency can be observed.

For this purpose, we used photogrammetry, which can be defined as a set of methods for determining the geometric properties of objects from photographic images. A new photogrammetric technique, called the structured light system technique (SLST) [11,12], has been developed in the last years. SLST allows three-dimensional surface reconstruction of objects with low cost and very high accuracy. SLST is used successfully in a variety of fields, such as surgery [13], industry [14], and aeronautics [15], or even in the documentation of cultural heritage [13,16–18]. Due to its specific characteristics of accuracy and cost, SLST seems the ideal technique to work together with the acoustic part to establish the noise abatement performance of any kind of AB—classical and SCAS—in sandy soils. The use of integrated photogrammetric-acoustic methods is not new and has been increasingly used in recent years in various fields of science and technology. Some examples of this use, without pretending to be exhaustive, have recently been proposed in the characterization of stone building materials, also using a laser scanner [19], in the reconstruction of natural and archeological underwater landscapes [20] or topography [21], to estimate the direction of drift and velocity of directional sonobuoys [22], for noise abatement in the design process of aircrafts in a wind tunnel [23], to develop a method to obtain dynamic three-dimensional modeling of channel tunnels [24], or finally to predict the collapse and instability of rocks' mass structure in echelon flaws [25].

Following this line, in this paper, we present a qualitative study to analyze the variation of the noise attenuation performance of different kinds of SCASs as a function of the sand accumulated in their basis, comparing these results with those obtained with a classical AB. To this end, we used an integrated photogrammetric-acoustic method consisting of (i) SLST to carefully determine the sand levels accumulated at the base of the different ABs analyzed, and (ii) an environmental acoustic measurement system to obtain the noise attenuation for each of the proposed cases. Furthermore, using this integrated method, we established a qualitative relationship between the movement of the accumulated sand and the attenuation obtained in all cases.

The article is organized as follows: In Section 2, we explain the theoretical basis of SLST. The specific details of the experimental set up, the characteristics of the samples, and the stages of the

measurement procedure are presented in Section 3. In Section 4, the results obtained are shown and discussed. Finally, the last section contains the concluding remarks, where the results are summarized.

2. Theoretical Basis

2.1. Photogrammetry

The method used to obtain three-dimensional measurements of the experimental model as a whole was automated photogrammetry, also known as photogrammetric correlation.

In order to understand the mathematical principles of the process of measuring from photographic images, it is first necessary to understand that this process of artificial reconstruction is based on the workings of the natural binocular vision of living beings (see Figure 2a). In that case, it could be considered that each element of the image captured by each eye could be represented by a line that joins three points: The center of the eye, the point of the retina, and the position of the object. The determination of the coordinates of the center of the eye and the point of the retina is not possible in the natural process of vision, but if the eye is replaced by a photographic camera and the image obtained is considered as the point of the retina, it is quite easy to obtain the coordinates of the line that passes through the following three points: The center of the projection of the camera (X_0, Y_0, Z_0), the point of the image (X_i, Y_i, Z_i), and the point of the ground (X, Y, Z), as one also can see in Figure 2a. With these conditions, each projective ray that represents the position of each point of the ground and its counterpart on the image can be expressed by means of the following equation:

$$\left. \begin{array}{ccc} X_i & Y_i & Z_i \\ X_0 & Y_0 & Z_0 \\ X & Y & Z \end{array} \right\} \rightarrow \frac{X_i - X_0}{X - X_0} = \frac{Y_i - Y_0}{Y - Y_0} = \frac{Z_i - Z_0}{Z - Z_0}. \quad (1)$$

From Equation (1) and considering Z_i as the focal length of the camera used, (f), the following expressions are obtained:

$$X_i = f \cdot \frac{[m_{11}(X - X_0) + m_{12}(Y - Y_0) + m_{13}(Z - Z_0)]}{[m_{31}(X - X_0) + m_{32}(Y - Y_0) + m_{33}(Z - Z_0)]}, \quad (2)$$

$$Y_i = f \cdot \frac{[m_{21}(X - X_0) + m_{22}(Y - Y_0) + m_{23}(Z - Z_0)]}{[m_{31}(X - X_0) + m_{32}(Y - Y_0) + m_{33}(Z - Z_0)]}. \quad (3)$$

These expressions relate the image coordinates (X_i, Y_i), with the coordinates of the center of the projection (X_0, Y_0, Z_0) and the ground coordinates (X, Y, Z). Note that a rotation matrix \mathbf{M} has been applied in order to place the photographic image in the same position in which it was made on the ground and to force, in this way, the intersection of the projective rays coming from each camera on the same point of the ground (A). Under these conditions, it is considered that the homologous straight line is the one that passes through the central projection points of the right camera (X_1, Y_1, Z_1), the point in the right image (X_d, Y_d, Z_d), and the same point of the ground (A) (X, Y, Z) [26]. An outline of this process can be seen in Figure 2b.

With two images the natural vision mechanism and can be artificially reconstructed and the coordinates of the photographed object can be obtained from the coordinates of the center of each camera and the coordinates of the object on the photographed image. Nowadays, the automatic processes of obtaining ground coordinates by photogrammetric correlation is known as structure from motion (SFM). More than two frames are involved in the process of calculating these coordinates. Thus, a third frame would be included the so-called trinocular epipolar condition [27], where a third projective ray with its origin in the center of the projection of a third camera would also intersect at the same point of the ground (A) as the other two projective rays, as can be seen in Figure 2c. In the same way, a fourth frame would include one more condition, called the quadrifocal epipolar condition [28,29], and so on (see Figure 2d). In this way, for each camera used, two equations would be

obtained for each point of the image (X_i, Y_i) , generating a system of equations for each point of the image from which its three-dimensional coordinates are obtained.

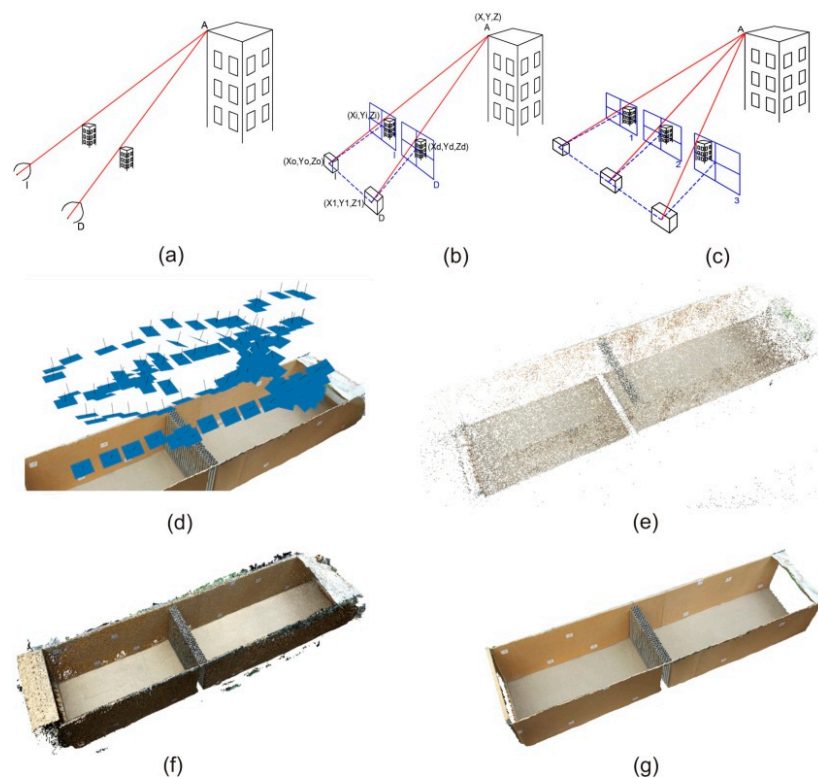


Figure 2. (a) Principle of natural stereoscopic vision; (b) Mechanism of artificial stereoscopic vision; (c) Epipolar trinocular condition for automatic correlation of three images; (d) Distribution of the images (in blue) used in one of the measurements of the experimental system. All the images shown meet the corresponding epipolar condition to be placed in the same relative position in which they were taken; (e) Result of a three-dimensional scattered point cloud; (f) Result of a dense three-dimensional point cloud; (g) A three-dimensional photorealistic model obtained after the generation of the triangular mesh and the texturing of its triangles.

The calculation algorithm to obtain the three-dimensional coordinates of an object using the SFM technique consists of the following phases [30]:

(i) Calibration of the photographic camera: Knowledge of the intrinsic parameters of the camera that define the conical projection of the obtained image is crucial to define the geometry of the image. These parameters are the focal distance, position of the main point, radial and tangential distortion, perpendicularity between axes, and pixel size and number of horizontal and vertical pixels. The calibration of the camera can be carried out in a previous process in which photographs are taken to already calibrated standards or, on the other hand, if a previous calibration is not carried out, the EXIF metadata file associated with the file of the digital image obtained can be used [31].

(ii) Identification of control points: The success of automatic photogrammetric correlation is the detection of common points in consecutive images. To do this, an initial adjustment is made to all the images to detect a series of common points and ensure that their relative position is the same as at the time of capture [32]. This first adjustment of the frames can be processed with mathematical algorithms, such as area based matching (ABM) defined as a correlation based on the area, or featured based matching (FBM), which is a correlation based on operators SIFT (scale invariant feature transform) and SURF (speeded-up robust features) [33].

(iii) Generation of a scattered three-dimensional points cloud: This phase is usually called bundle adjustment [34], where the first ground coordinates are obtained from the intersections of the straight

lines of each frame of a series of dispersed points of the photographed object. To do this, block adjustment of the coordinates of the centers of each camera, the control points, and those defined for the scattered cloud is carried out. Figure 2e shows the scattered points cloud obtained in the calculation of the three-dimensional model for the case of the thick screen.

(iv) Obtaining the dense point cloud: Starting from the orientation elements obtained in the adjustment of the dispersed cloud to improve the coordinates of the projection centers, the photogrammetric correlation is carried out pixel by pixel. For this purpose, algorithms of the type path-based multi-view stereo (PVMS) are used, which is based on an adjustment by least squares with geometric constraints [35]; multi image correspondance par méthodes automatiques de corrélation (MIC MAC), which allows the correlation of points from pyramidal images [26]; or semi-global matching (SGM), which performs calculations by pairs of images, as shown in Figure 2f [36].

(v) Reconstruction of the surface and texturing: Finally, and starting from the dense cloud of the points obtained, a three-dimensional mesh is made using triangles [37], which will be provided with the tonality that defines the photographic image for that area [38], obtaining realistic three-dimensional models (see an example in Figure 2g).

2.2. Acoustics

The behavior of an acoustic system is characterized by its transfer function, $H(f)$, which can be obtained as the Fourier transform of the impulse response, $h(t)$. If the impulse response is known, when the system is excited by an arbitrary input, the output signal can be calculated as follows:

$$o(t) = i(t) \otimes h(t) = \int_{-\infty}^{\infty} i(\tau) \cdot h(t - \tau) \cdot d\tau, \quad (4)$$

where $o(t)$ is the time domain output, $i(t)$ is the time domain input, and the symbol \otimes stands for convolution. Equation (2) can be translated to the frequency domain as follows:

$$O(f) = I(f) \cdot H(f), \quad (5)$$

where $O(f)$ is the output of the complex frequency domain and $I(f)$ is the input of the complex frequency domain. Assuming that the system is linear and invariable in time, the impulse response can be measured using a sine sweep signal. This technique has been employed for a long time for audio and acoustics measurements, but in the last two decades, it has become more popular within the scientific community, thanks to the computational capabilities of modern computers and the additional possibility of measuring simultaneously the distortion [39].

In our case, a sine sweep starting at 500 Hz and finishing at 20 kHz with a total length of 10 s was emitted by the loudspeakers in all the possible configurations (with and without the different ABs and after the movement of sand under wind conditions with every AB placed), and then recorded at the receiver position. The mathematical definition of the test signal is as follows:

$$x(t) = \sin \left[\frac{2\pi f_1}{\ln \frac{f_2}{f_1}} \cdot \left(e^{\frac{t}{T} \ln \frac{f_2}{f_1}} - 1 \right) \right], \quad (6)$$

where f_1 and f_2 are the lowest and the highest considered frequencies, respectively.

In order to obtain the impulse response in all the situations under analysis, the recorded signals have to be convolved with a filter that returns the impulse response. This is equivalent to a deconvolution. The filter is just a time reversal version of the excitation signal. We also considered the fact that the test signal does not have a white (flat) spectrum: Given that the instantaneous frequency sweeps slowly at low frequencies and much faster at high frequencies, the resulting spectrum is pink (falling down by -3 dB/octave). To compensate this coloration of the signal, a filter was used, applying a proper

amplitude envelope to the reversed sweep signal so that its amplitude now increases by +3 dB/octave. Figure 3b illustrates the impulse-response spectra obtained in two representative cases.

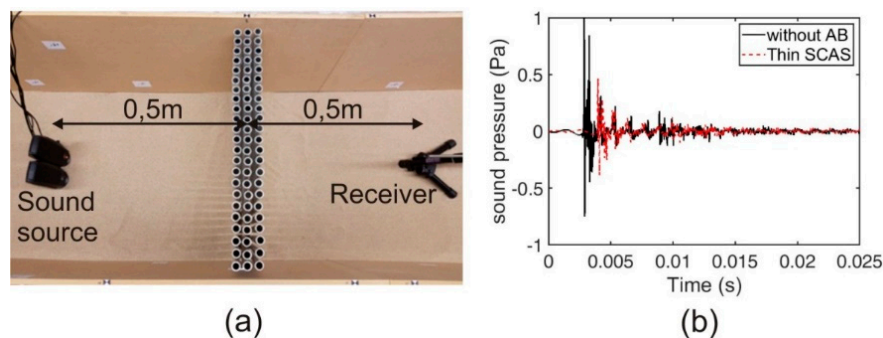


Figure 3. (a) Plan view of the experimental set up (loudspeakers and condenser microphone) and the position of the different ABs; (b) Examples of the impulse-response spectra for two cases: without AB (black solid line) and with thin Sonic Crystal Acoustic Screen (SCAS) (red dashed line).

The different impulse-response spectra have to be translated to the frequency space by a Fourier transform, averaged in frequency bands, and then the insertion loss can be calculated. Namely:

$$IL = 20 \cdot \log_{10} \left(\frac{p(\text{without barrier})}{p(\text{with barrier})} \right), \quad (7)$$

where p stands for the acoustic pressure.

The insertion loss (IL) parameter was used for the acoustic assessment. IL can be defined as the difference between the sound pressure level (L_P) created by the noise source, recorded at the same point with and without the AB:

$$IL = L_P(\text{without AB}) - L_P(\text{with AB}). \quad (8)$$

Figure 3a illustrates the positioning of the acoustic sources and the receiver near the considered AB.

3. Materials and Methods

As mentioned in the introduction, the main objective of the work was to measure, in a sandy environment, the acoustic attenuation obtained by different ABs (classics and SCASs) taking into account the sand accumulated at the base of each AB by airflow. The measurement of the amount of sand accumulated was done with SLST to obtain the most accurate values. In order to carry out this work, it was necessary to develop a complex prototype on a scale that allowed, under controlled conditions, the dragging of the sand by means of airflows, the subsequent measurements of its accumulation at the bottom part of the different ABs designed, and finally the acoustic evaluation of each prototype tested under the different conditions of sand accumulation.

This section presents the different materials used for the development of the designed prototype, divided into the following items: (i) Wind tunnel; (ii) selected sand; (iii) air fan and diffuser; (iv) AB and SCASs; (v) material used for the acoustic measurements; and (vi) material used to measure the sand distribution around the barriers.

3.1. Scaled Wind Tunnel

The scaled wind tunnel is the core of the experiment, and its function is to contain the sand when it is moved by the air fan, orienting it towards the ABs. It was designed in the form of a quadrangular prism resting on one of its lateral faces, and was uncovered both by the upper lateral face and by the two bases, as can be seen in Figure 4a,b. It was made of medium-density fiberboard (MDF).

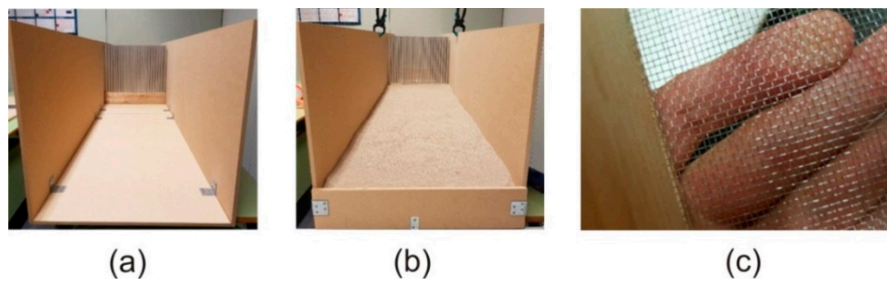


Figure 4. View of the scaled wind tunnel with a SCAS prototype (a) without sand and (b) with the sand reservoir used; (c) Sieve used for sand homogenization.

The scaled wind tunnel was formed by (i) 6 boards of 122 cm × 52 cm × 1 cm corresponding to three of the lateral surfaces of the square prism and (ii) 2 boards of 10 cm × 52 cm × 1 cm placed at the beginning and at the end of the tunnel (prism bases) to allow the storage of sand 10 cm deep. With these dimensions, the final size of the scaled wind tunnel constructed was 244 cm × 52 cm × 52 cm.

The panels were assembled and sealed with silicone to prevent the loss of sand through the junctions. At the end of the tunnel, a bag was located to store the sand expelled by the airflow created by the fan.

3.2. Sand

The scaled wind tunnel was designed with a reservoir to accumulate a 10 cm high amount of sand to cover its base. Taking into account the dimensions of this base (244 cm × 52 cm) and the average density of the beach sand used (1600 kg/m³), a total amount of 200 kg of sand was needed to fill the reservoir.

The use of beach sand implies the existence of sticks, algae, shells, and other unwanted objects. To eliminate these impurities and to homogenize the type of grain, the sand used in the experiment was sieved. The sieve used had a square mesh opening of 1 mm, with a Tyler mesh number (mesh/line) of 16 (see details in Figure 4c).

3.3. Fan and Air Diffuser

A set of preliminary tests were carried out to analyze the homogenization in the sand distribution along the scaled wind tunnel due to the airflow created by the fan used. An example of the results obtained can be seen in Figure 5a, where a trend of sand accumulation is observed on the right side of the wind tunnel. This phenomenon is caused by the airflow created by the movement of the blades, which in its encounter with the walls of the prototype creates a small turbulence on one side of the tunnel. To prevent this effect and to try make the prototype work with a more laminar flow similar to the one we can find in nature, an air diffuser was designed and built specifically to channel and laminate the airflow expelled by the fan.

The designed diffuser has two parts, and was prepared to fit into the tunnel inlet with a surface covering the diameter of the fan to channel most of the impelled airflow. The diffuser was designed to direct the airflow, and was made up of 12 movable sheets of wood 0.5 cm thick with a height of 40 cm high and 4 cm separation between them. Figure 5b,c shows different views of the final aspect of the constructed diffuser and its location in the prototype.

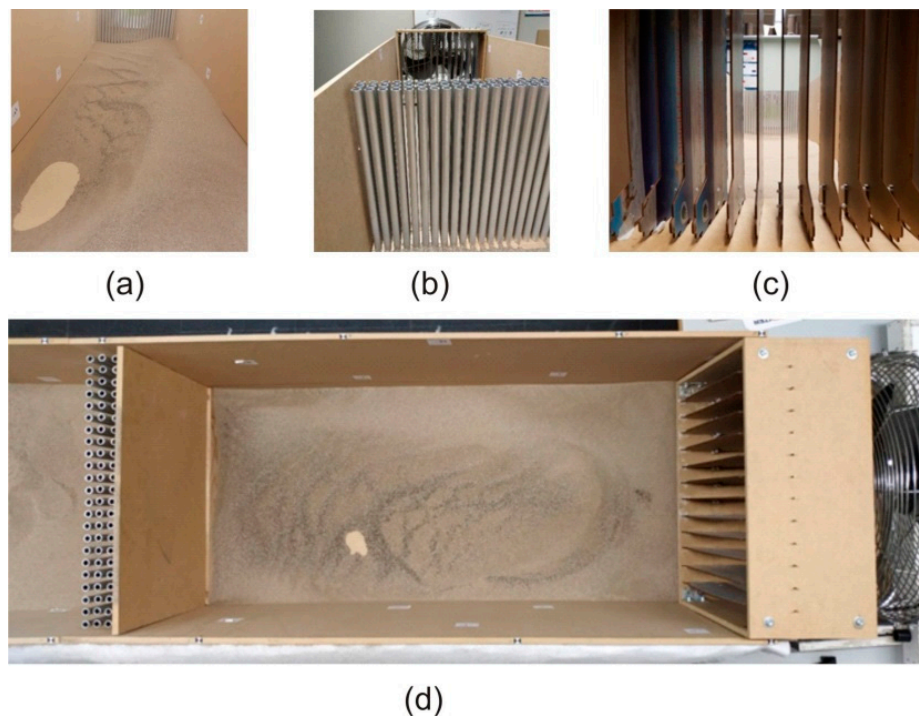


Figure 5. (a) Accumulation of sand on the right side of the tunnel caused by the turbulences of the fan blades before the insertion of the diffuser; (b) Front view of the diffuser in the final assembly; (c) Back view of the diffuser placed in the tunnel; (d) Plant view of the scaled wind tunnel.

3.4. Acoustic Screens Tested: Classical and Sonic Crystal Acoustic Screens

Three ABs, one classic and two based on the sonic crystals technology, were designed and built to carry out this work.

The classical AB, which by definition is a continuous wall, consisted of an MDF panel of $37.5\text{ cm} \times 52\text{ cm} \times 1\text{ cm}$ and was placed in such a way that the transversal section of the scaled wind tunnel was completely covered. This kind of AB is usually designed to attenuate noise in a wide range of frequencies due to its geometric characteristics, as it completely covers the line of sight between the sound source and the receiver, avoiding the transmission of noise.

On the other hand, and as previously explained in the introduction section, sonic crystals can be defined as a heterogeneous material formed by arrays of acoustic scatterers embedded in air. These materials present several properties related to the control of acoustic waves [40–42], but the main one related to noise attenuation and used in the design of ABs is the existence of bandgaps in the frequency domain. Bandgaps are frequency ranges where acoustic waves cannot be transmitted through sonic crystals, and their existence is due to Bragg's law [43,44]. Their size and position in the frequency domain depends on the geometric parameters of the sonic crystals, such as (i) the kind of crystalline array in which the scatterers are arranged, (ii) the distance between them (generally known as the lattice constant), or (iii) the surface area of the scatterers per surface unit of the crystalline lattice (called filling factor). This fact implies that, while classical ABs work to attenuate a wide part of the frequency spectrum, SCASs act as a filter, attenuating a specific and limited frequency range. The different way of working of both kinds of ABs (classical and SCAS) makes it very difficult to carry out a quantitative study on how the movement of sand in the bases of the ABs influences the acoustic attenuation achieved, since this attenuation is not comparable in any case.

The design of the SCASs used in this work was based on those most used one in the field of noise attenuation, which presents great symmetry and simplicity in their design [45]: Hollow cylindrical aluminum scatterers arranged in a square array. In order to have a greater variety of SCASs to be tested, two different diameters of the scatterers were considered, i.e., thick SCAS (larger diameter) and thin SCAS (smaller diameter). The design of these SCASs was made to real size and then adjusted to the dimensions of the wind tunnel, applying a scaling coefficient. In this study, the 1 kHz Bragg frequency was considered as the center of the bandgap, as it is the most important band in the normalized traffic noise spectrum [46]. With this condition, the lattice constant adopted was 17 cm and the diameter of the cylinders was 13.6 cm, for a filling factor of 0.5, appropriated for obtaining an acceptable bandgap size [44].

From the reference SCAS to the real size, the parameters were adjusted for a scaling factor of 1:8. Taking into account that the Bragg frequency would also be transferred according to the scale factor, the Bragg attenuation frequency for these scaled SCASs was in the 8 kHz band. By setting a filling factor of 0.25 (thin SCAS) and 0.45 (thick SCAS) to analyze the different cases, the resulting design parameters of both scaled SCAS are shown in Table 1.

Table 1. Design parameters of thin and thick barriers based on sonic crystals at a scaling factor of 1:8.

Name	Scaling Factor	Bragg Frequency (Hz)	Lattice Constant (cm)	Tube Diameter (cm)
Thin SCAS	1:8	8000	2.125	1.2
Thick SCAS	1:8	8000	2.125	1.6

Two commercial diameters of aluminum cylinders, 16 and 12 mm, were used for the design of the thick and thin SCASs, respectively. The SCASs prototypes were built to perfectly fit the cross section of the tunnel. To take into account the 10 cm deep sand reservoir, the cylinders were assembled on a wooden base of 52 cm × 10 cm × 10 cm. In Figure 6, the different geometric details of both scaled SCASs are shown.

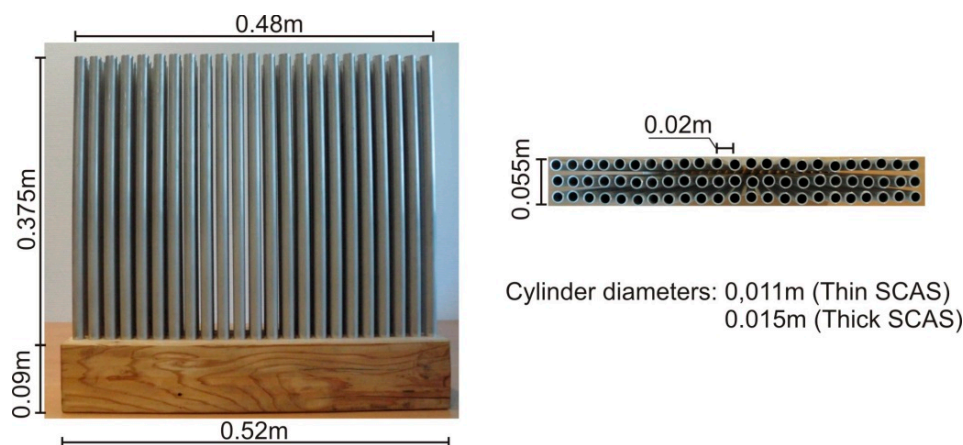






Figure 6. Front and plan view of the scaled SCASs.

3.5. Acoustic Measurements Equipment

The materials used for the evaluation of the *IL* of the different ABs basically consisted of a sound emitter, a sound card that allowed the audio signal to be digitized, and software that allowed both the creation of the emitted signal (sine sweep) and the recording of the audio tracks for further analysis. The details of this material can be seen in Table 2.

Table 2. Material used in acoustic measurements (*IL*).

Name	Image	Features
Loudspeakers		Total Watt (RMS): 2.2 W
Condenser microphone		Prepolarized Nominal Sensitivity 6 mV/Pa Frequency Response 10–20,000 Hz Class 1
Soundcard		XLR Inputs Signal to Noise Ratio: 97 dB THD+N: 0.005% Freq. Response: ± 0.35 dB
Software Cool Edit 2000		Record signal Manipulating signal Mix signal

3.6. Photogrammetric Measurements Equipment

The materials used to carry out the three-dimensional models and the corresponding measurements of the longitudinal sections of the topographic profiles adopted by the sand in each case of the ABs tested were (i) the photogrammetric correlation software Photoscan from Agisoft, (ii) TRIMBLE three-dimensional software for the treatment and management of point clouds, and (iii) a Canon EOS1DX MKIII camera, with a resolution of 21.1 Mpx, 35 mm format, Complementary Metal Oxide Semiconductor (CMOS) sensor, and a 50 mm lens for image acquisition.

4. Results

In this section, we analyze the results obtained in the experiments carried out with the different ABs prototypes designed on a scale of 1:8, and then extrapolate these results to a real scale of 1:1.

The experimental protocol was developed as follows: First, the sand reservoir of the scaled wind tunnel was filled with 10 cm of clean and sieved sand. The sand was flattened as much as possible to ensure that it was as horizontal as possible at all points in the wind tunnel. With this configuration, and without ABs located in the tunnel, the sound pressure was measured with the equipment indicated in Section 3.5. Next, and for each of the three considered ABs, photogrammetric and sound pressure measurements were made before and after connecting the scaled wind tunnel fan. The photogrammetric measurements investigated the sand permeability behavior of the three ABs. In the same way, the acoustic measurements allowed us to quantify the shift of the acoustic attenuation capability due to the variation of the sand relief for each of the ABs tested. In the different experiments, the fan worked for three hours in a row, which was the time needed to exhaust the sand tank.

The results obtained are divided into two categories, which are undoubtedly interrelated and not independent, but which will be explained separately for a better understanding of the data obtained and a simpler interpretation of the results. First, the permeability of the different ABs and their effect on sand movement will be evaluated. This aspect is particularly interesting if SCASs are to be installed in desert lands, for example, in infrastructures, such as the AVE Medina-La Meca in Saudi Arabia (Haramain High Speed Rail o HHR). In this type of terrain, the placement of classical ABs, formed by walls, can result in significant sand accumulation that endangers the transport infrastructures for which they are designed. However, SCASs would allow sand to pass through them, thus avoiding sand accumulation and protecting the infrastructure. This first analysis will allow us to quantify these accumulations for both types of ABs, the classics and the SCASs, under controlled conditions, as well as to make a first evaluation of the goodness of the SCASs with respect to the classical ABs in this sense. On the other hand, it is necessary to analyze the effect of sand accumulation on the acoustic efficiency of the different ABs considered. For this purpose, the acoustic attenuation of each AB was measured in each of the cases studied: Before and after the movement of sand due to the airflow created in the scaled wind tunnel. However, as we indicated in Section 3.4, the quantitative comparison of both types of ABs is very difficult due to the different ways they work acoustically. Therefore, here, we can only compare qualitatively the effect of sand on the attenuation properties of the AB classics and SCAS separately. However, this first study on the relationship between the movement of sand and the change in the acoustic attenuation properties of SCAS versus classical ABs may be very interesting for engineers to select the type of ABs to be installed in communication infrastructures depending on the type of ground.

4.1. Photogrammetric Results

In this section, we analyzed the sand permeability of the different AB prototypes considered. To this end, we compared the initial flat surface of the sand with its relief for each AB, after being subjected to the airflow of the wind tunnel, on both sides of each AB.

To quantitatively estimate the amount of sand moved in this comparison, we considered three longitudinal sections of the scaled wind tunnel (called sections 0.00, 0.26, and 0.52), as can be seen on the left side of Figure 7a. Only three longitudinal profiles were taken into account for this calculation since the displacement of the sand is regular, without large level differences in the wind tunnel cross-sections (in the direction of the ABs), due to the use of the air diffuser.

On the other hand, Figure 7b–d show, for each of the ABs considered, (i) the three longitudinal sections with the starting (black line) and modified (red line) sand profiles, (ii) section 0.26 indicating the clearing (pink color) and embankment (blue color) of the sand, and finally, (iii) a detail of this last section. In Figure 7, you can also see qualitatively the variation in the sand distribution in the front and behind each of the tested ABs, providing a clear picture of their permeability behavior.

The amount of sand moved due to airflow in the scaled wind tunnel for each AB case was calculated following the standard method of cubication in linear works, i.e., calculating the volume of sand moved in each clearing zone or embankment between each of the two sections considered. A diagram of how the measurements were made can be found on the right side of Figure 7a.

The results of the cubication performed are shown in Table 3. The analysis of this table leads to results that can be considered as expected. Thus, first, it is observed that in the classic AB, the main sand embankment takes place in its front part; that is, in the side exposed to the wind. The fact that classic ABs are formed by continuous walls, without openings, implies that the sand driven by the airflow accumulates in its front face, being practically insignificant in the back.

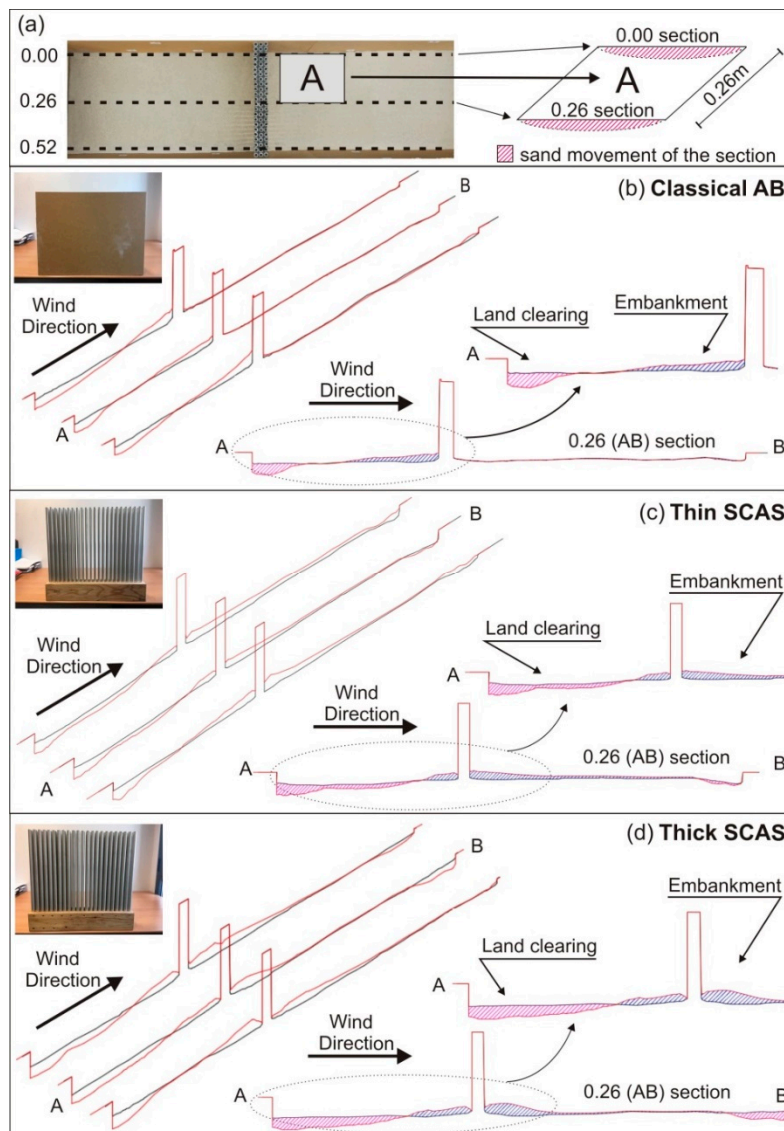


Figure 7. (a) Longitudinal sections used to evaluate the clearing or embankment of sand on both sides of each AB; (b–d) For each AB: the three longitudinal sections considered shown in perspective and the 0.26 profile image with an enlargement of the area close to the AB.

In the case of SCAS, the results are more interesting. First, it can be seen that the filling factor (index indicating the amount of mass of scatterers in the crystal) significantly affects the passage of sand. Thus, it can be observed that in the case of the thick SCAS, there is a 28.5% increase in the embankment of sand in its front part compared to what happens in the thin SCAS, with the filling factor of the first almost doubling that of the second (0.45 vs. 0.25). On the other hand, in the back part of the thick SCAS, the sand embankment produced is also larger than in the thin SCAS (11.6%). With these results, it can be concluded that increasing the filling factor in a SCAS will increase its sand accumulation capability and therefore its behavior will be more similar to that of classic ABs, increasing the “dune effect” that appears, with its maximum value in the front part of these last ones.

Table 3. Cubication of the sand displaced by the effect of the airflow in the scaled wind tunnel for each of the ABs tested both on a full scale (1:1) and on a scale of 1:8.

	Profiles	Volumes (m ³)			
		Front Part of the AB		Back Part of the AB	
		Clearing	Embankment	Clearing	Embankment
Classic AB	0.00–0.26	0.0030	0.0031	0.0008	0.0004
	0.26–0.52	0.0038	0.0027	0.0000	0.0004
	Scale 1:8	0.0068	0.0057	0.0008	0.0008
	Scale 1:1	0.0136	0.0114	0.0017	0.0016
Thin SCAS	0.00–0.26	0.0035	0.0018	0.0003	0.0067
	0.26–0.52	0.0088	0.0016	0.0010	0.0033
	Scale 1:8	0.0123	0.0034	0.0012	0.0100
	Scale 1:1	0.0246	0.0068	0.0025	0.0200
Thick SCAS	0.00–0.26	0.0051	0.0026	0.0010	0.0058
	0.26–0.52	0.0065	0.0022	0.0015	0.0055
	Scale 1:8	0.0116	0.0047	0.0024	0.0113
	Scale 1:1	0.0231	0.095	0.0049	0.0226

4.2. Acoustic Results

In this section, we analyzed how the change in the relief of the sand due to airflow influences the acoustic attenuation capability of the tested ABs.

To do that, we calculated the *IL* index for every AB as a function of the frequency before and after the change in the sand relief due to the airflow. The results can be seen in Figure 8, where the comparison of *IL* for each AB before (red line) and after (black line) airflow is presented, both on the scale of the experiment (1:8) and on a real scale (1:1).

In the case of the classical AB (Figure 8a), we can observe that a generalized decrease of *IL* is produced at the frequency range considered after the airflow, when an improvement of the sand accumulation on the front side of the AB is produced, except in the 350 to 500 Hz range where a slight improvement of the *IL* before the airflow appears.

To analyze the acoustic attenuation behavior of SCASs, it is worth remembering that they were geometrically designed in such a way that the bandgap must appear around 1 kHz, which in the scale model is transferred to an 8 kHz bandgap. This means that the only attenuation we must take into account is the one that appears in this band, because it is the one that is directly related to the behavior of the sonic crystal. No other possible attenuations that appear in the spectra and that are not directly due to the action of the sonic crystals were considered in this work. In the *IL* spectra of both SCASs, shown in Figure 8b,c, an interesting effect in their attenuation properties appears: The size of the bandgap increases after the airflow when the sand is accumulated on the basis of the SCAS, regardless of the value of filling factor. Thus, this effect can be considered as robust although it is especially evident for the higher filling fraction, as the thick SCAS achieves a very noticeable increase in *IL* around the bandgap frequency of 8 kHz (1 kHz at the real scale) and up to 5 dB, while the thin SCAS prototype presents an increase of only 2 to 3 dB around this bandgap frequency.

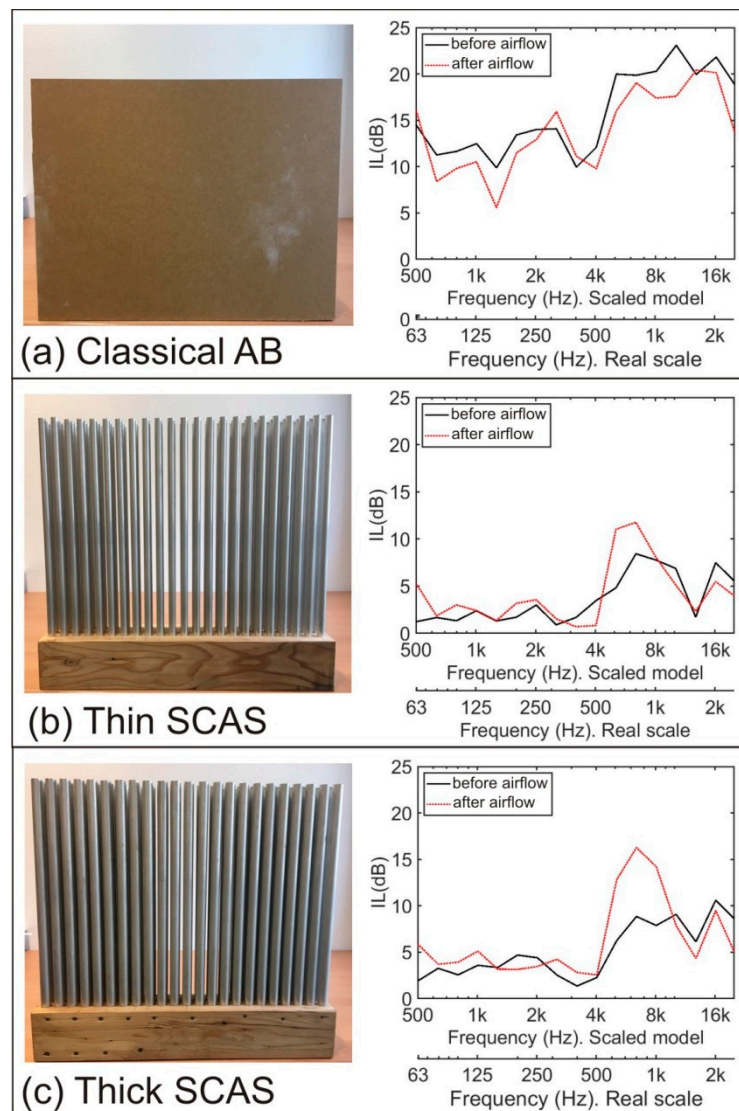


Figure 8. (a–c) On the left side of the figures you can see a picture of the AB considered in this study; on the right side we show the *IL* spectra as a function of the frequency for each case before (black continuous line) and after (red dotted line) to apply the air flow.

5. Conclusions

In this work, we presented a mixed photogrammetric-acoustic technique to carefully analyze, together with the design and construction of a scale wind tunnel, the attenuation behavior and the permeability to sand of a new type of acoustic barriers based on periodic arrays of scatterers, usually called sonic crystal acoustic screens. In contrast to the non-permeability properties of classic barriers, the screens based on sonic crystal allow permeability to wind and water, but until now, no one has analyzed the sand permeability and its influence on sound attenuation. This situation is especially interesting for infrastructures located in desert soils.

The development of the work was complex, because quantitative comparison of the results in both types of ABs is very difficult due to the different ways they work acoustically. Therefore, for this first study on the relationship between sand movement and the change in the acoustic attenuation properties of SCAS versus classical ABs, we preferred to focus on a qualitative analysis, which may already be of interest to engineers when selecting the type of ABs to be installed in communications infrastructure depending on the type of soil.

Thus, we experimentally verified that (i) the permeability of these screens to sand is high, allowing its passage and avoiding the accumulation of sand at the base of these devices forming dunes, as happens in the case of classic screens; and (ii) in this new kind of barrier, the attenuation performance increases as a function of the filling factor when the sand accumulates at the base of the screens, which is unlike what happens with traditional screens, which decreases when the sand is accumulated. Although the physical reasons for this behavior are not yet known, this seems very interesting from an engineering point of view.

However, more funds are needed to build a battery of sonic crystal acoustic screen prototypes in order to analyze their permeability and acoustic performance in the scaled wind tunnel. At the same time, it seems necessary to improve the scaled wind tunnel in order to obtain better performance, for example, to increase the sand storage capability and analyze the distribution of sand in a higher period of time. In addition, it will be necessary to carry out more studies in free field conditions and to develop powerful simulators to understand and use the mechanisms that generate the increase in attenuation performance due to the accumulation of sand at the base of this kind of screen.

Author Contributions: J.M.B. wrote the paper and designed the experiment. F.B.-M. wrote the paper and photogrammetry methodology. J.R. provided the initial idea, acoustic measurements and wrote the paper. M.F. wrote the paper, formal analysis and developed the acoustical theory. J.V.S.-P. project administration, funding acquisition and writing—review and editing.

Conflicts of Interest: The authors declare no conflict of interest.

References

1. EC Directive. *Directive 2002/49/EC of the European Parliament and of the Council of 25 June 2002 Relating to the Assessment and Management of Environmental Noise*; Communities L 189 (2002); Official J. Eur.: Brussels, Belgium, 2002.
2. Department of Transportation, Federal Highway Administration USA. *Keeping the Noise Down, Highway Traffic Noise Barriers*; Federal Highway Administration USA: Washington, DC, USA, 2001. Available online: https://www.fhwa.dot.gov/environment/noise/noise_barriers/design_construction/keepdown.cfm (accessed on 2 September 2019).
3. Castiñeira-Ibañez, S.; Rubio, C.; Sánchez-Pérez, J.V. Environmental noise control during its transmission phase to protect buildings. Design model for acoustic barriers based on arrays of isolated scatterers. *Build. Environ.* **2015**, *93*, 179–185. [[CrossRef](#)]
4. Fredianelli, L.; Del Pizzo, A.; Licitra, G. Recent Developments in Sonic Crystals as Barriers for Road Traffic Noise Mitigation. *Environments* **2019**, *6*, 14. [[CrossRef](#)]
5. Martínez-Sala, R.; Sancho, J.; Sánchez-Pérez, J.V.; Gómez, V.; Llinares, J.; Meseguer, F. Sound attenuation by sculpture. *Nature* **1995**, *378*, 241. [[CrossRef](#)]
6. Morandi, F.; Miniaci, M.; Marzani, A.; Barbaresi, L.; Garai, M. Standardised acoustic characterisation of sonic crystals noise barriers: Sound insulation and reflection properties. *Appl. Acoust.* **2016**, *114*, 294–306. [[CrossRef](#)]
7. Castiñeira-Ibañez, S.; Rubio, C.; Romero-García, V.; Sánchez-Pérez, J.V.; García-Raffi, L.M. Design, Manufacture and Characterization of an Acoustic Barrier Made of Multi-Phenomena Cylindrical Scatterers Arranged in a Fractal-Based Geometry. *Arch. Acoust.* **2012**, *37*, 455–462. [[CrossRef](#)]
8. Castiñeira-Ibañez, S.; Romero-García, V.; Sánchez-Pérez, J.V.; García-Raffi, L.M. Periodic systems as road traffic noise reducing devices: prototype and standardization. *Environ. Eng. Manag. J.* **2015**, *14*, 2759–2769. [[CrossRef](#)]
9. Wang, Y.F.; Wang, Y.S.; Laude, V. Wave propagation in two-dimensional viscoelastic metamaterials. *Phys. Rev. B* **2015**, *92*, 104110. [[CrossRef](#)]
10. Wang, Y.F.; Liang, J.W.; Chen, A.L.; Wang, Y.S.; Laude, V. Wave propagation in one-dimensional fluid-saturated porous metamaterials. *Phys. Rev. B* **2019**, *99*, 134304. [[CrossRef](#)]
11. Valkenburg, R.J.; Mcivor, A.M. Accurate 3D measurement using a structured light system. *Image Vis. Comput.* **1998**, *16*, 99–110. [[CrossRef](#)]

12. Hui, Z.; Liyan, Z.; Hongtao, W.; Jianfu, C. Surface measurement based on instantaneous random illumination. *Chin. J. Aeronaut.* **2008**, *22*, 316–324. [[CrossRef](#)]
13. McPherron, S.P.; Gernat, T.; Hublin, J.J. Structured light scanning for high-resolution documentation of in situ archaeological finds. *J. Archaeol. Sci.* **2009**, *36*, 19–24. [[CrossRef](#)]
14. Bruno, F.; Bianco, G.; Muzzupappa, M.; Barone, S.; Rationale, A.V. Experimentation of structured light and stereo vision for underwater 3D reconstruction. *ISPRS J. Photogramm.* **2011**, *66*, 508–518. [[CrossRef](#)]
15. Bertani, D.; Cetica, M.; Melozzi, M.; Pezzati, L. High-Resolution optical topography applied to ancient painting diagnostics. *Opt. Eng.* **1995**, *34*, 1219–1225. [[CrossRef](#)]
16. Buchón-Moragues, F.; Bravo, J.M.; Ferri, M.; Redondo, J.; Sánchez-Pérez, J.V. Application of structured light system technique for authentication of wooden panel paintings. *Sensors* **2016**, *16*, 881. [[CrossRef](#)] [[PubMed](#)]
17. Arias, P.; Herraez, J.; Lorenzo, H.; Ordoñez, C. Control of structural problems in cultural heritage monuments using close-range photogrammetry and computer methods. *Comput. Struct.* **2005**, *83*, 1754–1766. [[CrossRef](#)]
18. Rocchini, C.; Cignoni, P.; Montani, C.; Pingi, C.; Scopigno, R.A. Low cost 3D scanner based on structured light. *Comput. Graph. Forum* **2002**, *20*, 299–308. [[CrossRef](#)]
19. Bianchi, M.G.; Casula, G.; Cuccuru, F.; Fais, S.; Ligas, P.; Ferrara, C. Three-dimensional imaging from laser scanner, photogrammetric and acoustic non-destructive techniques in the characterization of stone building materials. *Adv. Geosci.* **2018**, *45*, 57–62. [[CrossRef](#)]
20. Mattei, G.; Troisi, S.; Aucelli, P.P.C.; Pappone, G.; Peluso, F.; Stefanile, M. Multiscale reconstruction of natural and archaeological underwater landscape by optical and acoustic sensors. In Proceedings of the 2018 IEEE International Workshop on Metrology for the Sea, Bari, Italy, 8–10 October 2018; Learning to Measure Sea Health Parameters (MetroSea): Bari, Italy; pp. 46–49.
21. Alvarez, L.V.; Moreno, H.A.; Segales, A.R.; Pham, T.G.; Pillar-Little, E.A.; Chilson, P.B. Merging Unmanned Aerial Systems (UAS) Imagery and Echo Soundings with an Adaptive Sampling Technique for Bathymetric Surveys. *Remote Sens.* **2018**, *10*, 1362. [[CrossRef](#)]
22. Miller, B.S.; Wotherspoon, S.; Rankin, S.; Calderan, S.; Leaper, R.; Keating, J.L. Estimating drift of directional sonobuoys from acoustic bearings. *J. Acoust. Soc. Am.* **2018**, *143*, 25–30. [[CrossRef](#)] [[PubMed](#)]
23. Shortis, M.R.; Robson, S.; Jones, T.W.; Goad, W.K.; Lunsford, C.B. Photogrammetric tracking of aerodynamic surfaces and aerospace models at nasa langley research center. In Proceedings of the ISPRS Annals of the Photogrammetry, Remote Sensing and Spatial Information Sciences, Volume III-5, 2016 XXIII ISPRS Congress, Prague, Czech, 12–19 July 2016; pp. 27–34.
24. Moisan, E.; Heinkele, C.; Charbonnier, P.; Foucher, P.; Grussenmeyer, P.; Guillemin, S.; Koehl, M. Dynamic 3d modeling of a canal-tunnel using photogrammetric and bathymetric data. In Proceedings of the 2017 3D Virtual Reconstruction and Visualization of Complex Architectures, Nafplio, Greece, 1–3 March 2017.
25. Zhang, D.; Li, S.; Bai, X.; Yang, Y.; Chu, Y. Experimental Study on Mechanical Properties, Energy Dissipation Characteristics and Acoustic Emission Parameters of Compression Failure of Sandstone Specimens Containing En Echelon Flaws. *Appl. Sci.* **2019**, *9*, 596. [[CrossRef](#)]
26. Kraus, K. *Photogrammetry: Geometry from Images and Laser Scans*, 2nd ed.; Walter de Gruyter: Berlin, Germany, 2000; Volume 1, pp. 4–27.
27. Bhalerao, R.H.; Gedam, S.S.; Almansa, A. Fast epipolar resampling of trinocular linear scanners images using Chandrayaan-1 TMC dataset. In Proceedings of the 2013 IEEE Second International Conference on Image Information Processing (ICIIP-2013), Shimla, India, 9–11 December 2013; pp. 12–16.
28. Hartley, R.I.; Schaffalitzky, F. Reconstruction from projections using grassmann tensors. *IJCV* **2009**, *83*, 274–293. [[CrossRef](#)]
29. Rodríguez López, A.L. Algebraic Epipolar Constraints for Efficient Structureless Multiview Motion Estimation. Ph.D. Thesis, Faculty of Informatics, University of Murcia, February 2013.
30. Ahmadabadian, A.H.; Robson, S.; Boehm, J.; Shortis, M.; Wenzel, K.; Fritsch, D. A comparison of dense matching algorithms for scaled surface reconstruction using stereo camera rigs. *PRS* **2013**, *78*, 157–167. [[CrossRef](#)]
31. Goesele, M.; Snavely, N.; Curless, B.; Hoppe, H.; Seitz, S.M. Multi-view stereo for community photo collections. In Proceedings of the 2007 IEEE 11th International Conference on Computer Vision, Janeiro, Brazil, 14–20 October 2007; pp. 1–8.
32. Harvey, E.S.; Shortis, M.R. Calibration stability of an underwater stereo-video system: implications for measurement accuracy and precision. *MTS* **1998**, *32*, 3–17.

33. Babbar, G.; Bajaj, P.; Chawla, A.; Gogna, M. Comparative study of image matching algorithms. *IJITKM* **2010**, *2*, 337–339.
34. Triggs, B.; McLauchlan, P.F.; Hartley, R.I.; Fitzgibbon, A.W. Bundle adjustment a modern synthesis. In *International Workshop on Vision Algorithms*; Springer: Berlin/Heidelberg, Germany, 1999; pp. 298–372.
35. Olague, G.; Dunn, E. Development of a practical photogrammetric network design using evolutionary computing. *Photogramm. Rec.* **2007**, *22*, 22–38. [[CrossRef](#)]
36. Hirschmuller, H. Stereo processing by semiglobal matching and mutual information. *IEEE T Pattern Anal.* **2007**, *30*, 328–341. [[CrossRef](#)] [[PubMed](#)]
37. Salomon, D. Bezier approximation. In *Curves and Surfaces for Computer Graphics*; Springer Science & Business Media: Northridge, CA, USA, 2007; pp. 175–250.
38. Öhrn, K. Different Mapping Techniques for Realistic Surfaces. Ph.D. Thesis, University of Gävle, Gävle, Sweden, June 2008.
39. Farina, A. Simultaneous measurement of impulse response and distortion with a swept-sine technique. In Proceedings of the Audio Engineering Society Convention 108, Paris, France, 19–22 February 2000; p. 5093.
40. Chen, Y.; Lifeng, W. Periodic co-continuous acoustic metamaterials with overlapping locally resonant and Bragg band gaps. *Appl. Phys. Lett.* **2014**, *105*, 191907. [[CrossRef](#)]
41. Kaina, N.; Causier, A.; Bourlier, Y.; Fink, M.; Berthelot, T.; Lerosey, G. Slow waves in locally resonant metamaterials line defect waveguides. *Sci. Rep.* **2017**, *7*, 15105. [[CrossRef](#)] [[PubMed](#)]
42. Cummer, S.A.; Christensen, J.; Alù, A. Controlling sound with acoustic metamaterials. *Nat. Rev. Mater.* **2016**, *1*, 16001. [[CrossRef](#)]
43. Sigalas, M.M.; Economou, E.N. Elastic and acoustic wave band structure. *J. Sound Vib.* **1992**, *158*, 377. [[CrossRef](#)]
44. Sánchez-Pérez, J.V.; Caballero, D.; Martínez-Sala, R.; Rubio, C.; Sánchez-Dehesa, J.; Meseguer, F.; Llinares, J.; Gálvez, F. Sound Attenuation by a Two-Dimensional Array of Rigid Cylinders. *Phys. Rev. Lett.* **1998**, *80*, 5325. [[CrossRef](#)]
45. Sánchez-Pérez, J.V.; Rubio, C.; Martínez-Sala, R.; Sanchez-Grandia, R.; Gomez, V. Acoustic barriers based on periodic arrays of scatterers. *Appl. Phys. Lett.* **2002**, *81*, 5240. [[CrossRef](#)]
46. European Committee for Standardisation, EN 1793-3 (1997). *Road Traffic Noise Reducing Devices—Test Method for Determining the Acoustic Performance—Part 3: Normalised Traffic Noise Spectrum*; CEN: Brussels, Belgium, 1997.



© 2019 by the authors. Licensee MDPI, Basel, Switzerland. This article is an open access article distributed under the terms and conditions of the Creative Commons Attribution (CC BY) license (<http://creativecommons.org/licenses/by/4.0/>).